Article

Bevel-edge epitaxy of ferroelectric rhombohedral boron nitride single crystal

https://doi.org/10.1038/s41586-024-07286-3

Received: 17 July 2023

Accepted: 8 March 2024

Published online: 1 May 2024

Check for updates

Li Wang[1,15]✉, Jiajie Qi[2,15], Wenya Wei[3,15], Mengqi Wu[4,15], Zhibin Zhang[2], Xiaomin Li[1], Huacong Sun[1,5], Quanlin Guo[2], Meng Cao[1], Qinghe Wang[2], Chao Zhao[6], Yuxuan Sheng[7], Zhetong Liu[8], Can Liu[9], Muhong Wu[8,10,14], Zhi Xu[11], Wenlong Wang[1,11], Hao Hong[2,10], Peng Gao[8], Menghao Wu[7], Zhu-Jun Wang[12], Xiaozhi Xu[3], Enge Wang[1,10,11,13], Feng Ding[6]✉, Xiaorui Zheng[4]✉, Kaihui Liu[2,10,11]✉ & Xuedong Bai[1,5,11]✉

Within the family of two-dimensional dielectrics, rhombohedral boron nitride (rBN) is considerably promising owing to having not only the superior properties of hexagonal boron nitride[1–4]—including low permittivity and dissipation, strong electrical insulation, good chemical stability, high thermal conductivity and atomic flatness without dangling bonds—but also useful optical nonlinearity and interfacial ferroelectricity originating from the broken in-plane and out-of-plane centrosymmetry[5–23]. However, the preparation of large-sized single-crystal rBN layers remains a challenge[24–26], owing to the requisite unprecedented growth controls to coordinate the lattice orientation of each layer and the sliding vector of every interface. Here we report a facile methodology using bevel-edge epitaxy to prepare centimetre-sized single-crystal rBN layers with exact interlayer ABC stacking on a vicinal nickel surface. We realized successful accurate fabrication over a single-crystal nickel substrate with bunched step edges of the terrace facet (100) at the bevel facet (110), which simultaneously guided the consistent boron–nitrogen bond orientation in each BN layer and the rhombohedral stacking of BN layers via nucleation near each bevel facet. The pure rhombohedral phase of the as-grown BN layers was verified, and consequently showed robust, homogeneous and switchable ferroelectricity with a high Curie temperature. Our work provides an effective route for accurate stacking-controlled growth of single-crystal two-dimensional layers and presents a foundation for applicable multifunctional devices based on stacked two-dimensional materials.

Among the existing methods, successful control of the growth of boron nitride (BN) layers typically focuses on the lattice orientation of the monolayer and the thickness of the multilayer[27–36]. For instance, wafer-sized single-crystal monolayer films have been grown through seamless stitching of self-collimated BN domains on liquid gold[31] or unidirectionally aligned BN domains on a surface-symmetry-broken substrate with parallel atomic steps[32,33]. Thick layers of hexagonal boron nitride (hBN) can be prepared on metal substrates with high solubility and catalytic activity of specific precursors[36] or on insulating substrates at very high growth temperatures[37]. Recently, the preparation of a single-crystal hBN trilayer film was realized on nickel (Ni) foil with parallel atomic steps, achieving a substrate that combines high catalytic activity with broken surface symmetry[35]. However, the growth of large-sized single-crystal rhombohedral boron nitride (rBN) films with an appropriate thickness has remained unattainable until now. The main challenge of fabrication is that the rBN phase is metastable and the hBN phase is stable[38]. Owing to the different electronegativities of the boron (B) and nitrogen (N) atoms in the BN lattice, the B (N) atom in a layer prefers to directly align with the N (B) sites of the adjacent layers. Such a configuration endows the hBN phase with inherent stability and consequently the prevailing predominance in most conventional growth[39,40].

In principle, the growth of rBN layers has two prerequisites: (1) breaking the energetically preferential couplings between interlayer B and N atoms at every interface to realize a single direction of B–N bonds in each layer; and (2) guiding accurate lattice sliding with a constant integer multiple of half the B–N bond length along the armchair direction of each layer to ensure interlayer ABC stacking of the pure rBN

[1]Institute of Physics, Chinese Academy of Sciences, Beijing, China. [2]State Key Laboratory for Mesoscopic Physics, Frontiers Science Centre for Nano-optoelectronics, School of Physics, Peking University, Beijing, China. [3]Guangdong Provincial Key Laboratory of Quantum Engineering and Quantum Materials, School of Physics, South China Normal University, Guangzhou, China. [4]School of Engineering, Westlake University, Hangzhou, China. [5]School of Physical Sciences, University of Chinese Academy of Sciences, Beijing, China. [6]Shenzhen Institute of Advanced Technology, Shenzhen, China. [7]School of Physics, Huazhong University of Science and Technology, Wuhan, China. [8]International Centre for Quantum Materials, Collaborative Innovation Centre of Quantum Matter, Peking University, Beijing, China. [9]Key Laboratory of Quantum State Construction and Manipulation (Ministry of Education), Department of Physics, Renmin University of China, Beijing, China. [10]Interdisciplinary Institute of Light-Element Quantum Materials and Research Centre for Light-Element Advanced Materials, Peking University, Beijing, China. [11]Songshan Lake Materials Laboratory, Dongguan, China. [12]School of Physical Science and Technology, ShanghaiTech University, Shanghai, China. [13]Tsientang Institute for Advanced Study, Hangzhou, China. [14]Present address: Songshan Lake Materials Laboratory, Dongguan, China. [15]These authors contributed equally: Li Wang, Jiajie Qi, Wenya Wei, Mengqi Wu. ✉e-mail: liwang@iphy.ac.cn; f.ding@siat.ac.cn; zhengxiaorui@westlake.edu.cn; khliu@pku.edu.cn; xdbai@iphy.ac.cn

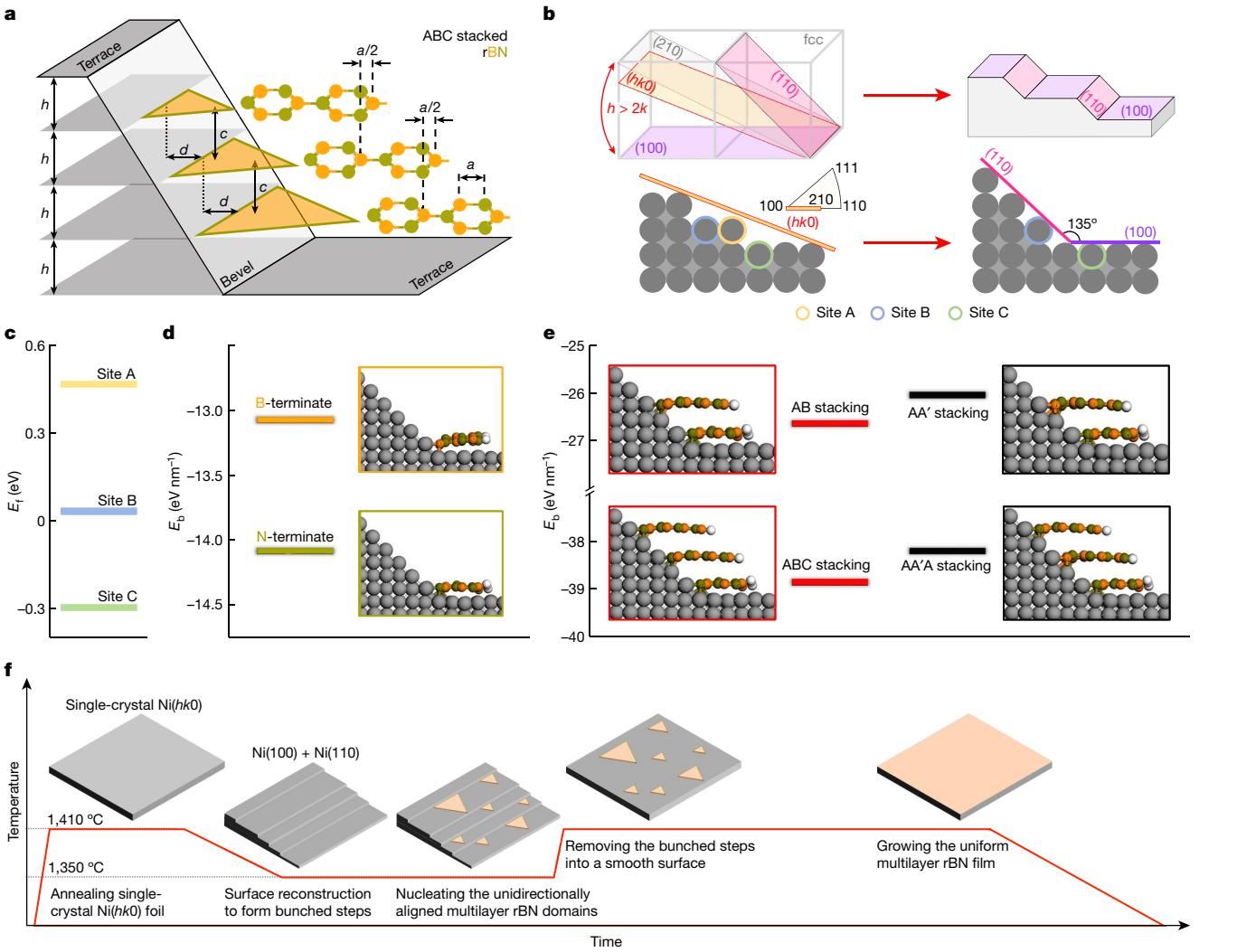

Fig. 1 | Design of bevel-edge-guided growth of single-crystal rBN layers. **a**, Scheme of the designed bevel edge to simultaneously control the lattice orientation of each layer and the interlayer sliding distance of rBN. Here, *a* and *c* indicate the single B–N bond length and interlayer spacing of rBN, respectively, and *h* and *d* are the interlayer spacing of the terrace facets and the horizontal distance of adjacent edges at the bevel facet, respectively. **b**, Scheme of the reconstruction from Ni(*hk*0) to bunched steps consisting of terrace facet Ni(100) and bevel facet Ni(110). **c**, The corresponding formation energy (E_f) of the Ni atom at the site shown in **b**. **d**,**e**, Binding energies (E_b) of BN monolayer (**d**) and multilayer (**e**) nuclei attached to the bevel facet of Ni(110) on bunched steps, showing that ABC-stacking rBN domains are energetically preferred on the substrate with designed bunched steps. **f**, Diagram of five typical stages in the growth of a single-crystal rBN multilayer film with uniform thickness. In this figure, orange, green, grey and white balls represent the B, N, Ni and H atoms, respectively.

phase (Fig. 1a). In our design, growth substrates with bunched step edges consisting of selected terrace and bevel facets were used. The strong couplings between the bunched step edges at the bevel plane and the edges of the BN lattice leads to the nucleation of each BN layer from the bevel facet and their unidirectional alignment. In addition, the appropriate slope of the bevel plane to terrace plane further ensures the sliding of constant integer times half the B–N bond length along the armchair direction to ultimately achieve the desired interlayer ABC-stacking sequence. Thus, single-crystal pure-phase rBN films were successfully grown.

For a practical substrate design, we need to minimize the mismatch between the rBN lattice and bunched steps to the greatest extent possible. In principle, both the candidates of terrace and bevel facets in bunched steps are 'low index' options, that is, Ni(100), Ni(110) and Ni(111). Geometrically, Ni(100) is the optimal terrace facet for adapting to the layer spacing of rBN (Extended Data Fig. 1a), and Ni(110) is the best bevel facet for guiding sliding with about 2.5 times the B–N bond length along the armchair direction at the interface (Extended Data Fig. 1b). Experimentally, the specific terrace and bevel morphology mentioned above could be obtained through surface reconstruction of the Ni(*hk*0) facet, where $h > 2k$. On such a surface, the existence of relatively unstable Ni atoms at the inherent atomic step-edge sites on such 'high index' facets will drive the surface to reconstruct and form the flat terrace Ni(100) and bevel Ni(110) facets (Fig. 1b,c), because they have a much higher probability for volatilizing from the surface in a high-temperature (close proximity to the surface pre-melting state) and low-pressure environment. The requirement of $h > 2k$ ensures that the facet Ni(*hk*0) is more inclined towards the terrace facet of Ni(100) and bevel facet of Ni(110). Theoretical analysis reveals that the couplings between the N-terminated zigzag edge of BN and the bunched step edges at bevel facet Ni(110) is energetically preferred (Fig. 1d). This implies a mechanism of bevel-edge epitaxy in which all BN layers nucleating from the bevel facet could maintain the exact same orientation or zero twisting angle between neighbouring layers, which excludes the formation of hBN with AA′A stacking order. For multilayer nuclei, as designed, ABC stacking has the minimum-energy

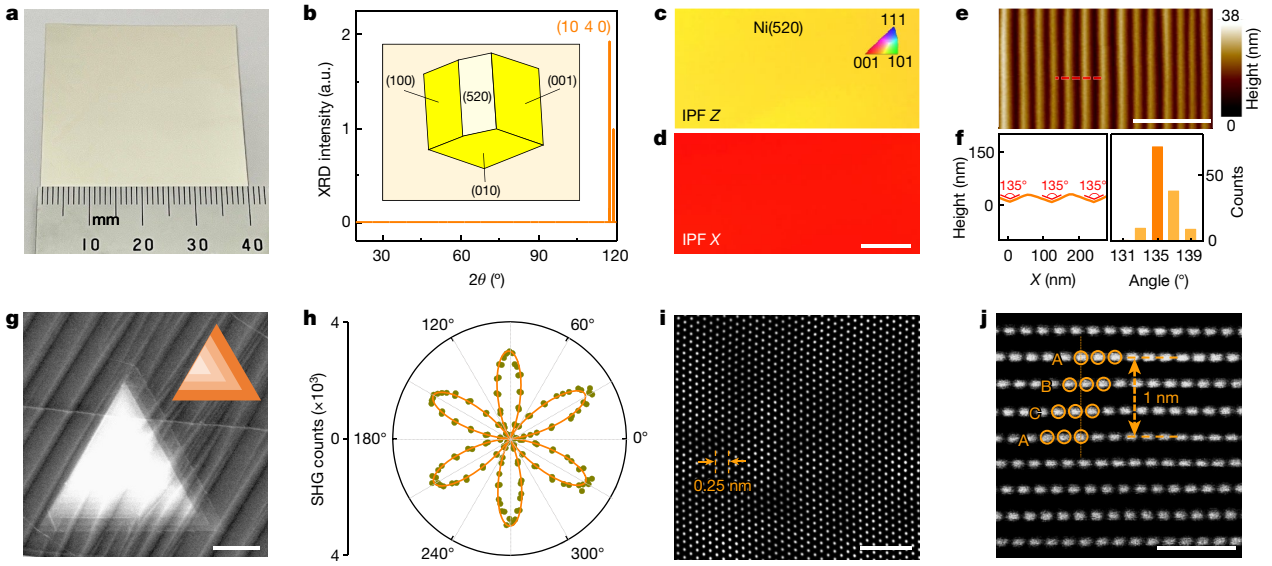

Fig. 2 | Growth and characterization of rBN layers. a, Photograph of a 4 × 4-cm^2 Ni(520) single crystal. **b**, XRD 2θ-scan pattern of annealed Ni foil with the (520) facet orientation. Here, the sharp (10 4 0) peak represents the Ni(520) facet, since only facets with all Miller indices even or odd give a non-zero XRD-2θ scan signal owing to the extinction rule. Inset: the reconstructed single-crystal XRD data for the Ni(520) foil. **c**,**d**, EBSD inverse pole figure (IPF) mappings along the Z (**c**) and X (**d**) directions, respectively, confirming the single crystallinity of Ni(520) foil without in-plane rotation. The two images are the same size. **e**, Typical AFM topographic mapping of the as-annealed Ni surface after the surface reconstruction stage. **f**, Height profile (left) corresponding to the red dotted line in **e** and the statistics of relative angles between the terrace and bevel facets (right), indicating that the obtained bunched steps have angles of about 135° over a large area. **g**, Representative scanning electron microscopy (SEM) image of the rBN domain on the stepped Ni(520) surface. Inset: scheme of the parallelly stacked BN layers attached to the bunched step edge. **h**, Polarized SHG pattern of as-grown rBN layers with six-fold symmetry, showing the absence of twisted layer with small angle. **i**, Atomically resolved HAADF-STEM image of as-grown rBN layers, where the in-plane lattice constant is measured to be 0.25 nm. **j**, Cross-sectional STEM image of rBN, demonstrating the ABC stacking of the as-grown rBN layers, where the orange circles represent the unit cells of rBN layers. The zone axis here is the zigzag direction of the rBN layers. Scale bars, 100 μm (**d**), 500 nm (**e**), 10 μm (**g**), 1 nm (**i**,**j**).

state compared with AA′A stacking (Fig. 1e). Furthermore, the flat bevel facet could lock the sliding direction of each layer, thereby preventing the formation of unwanted ABA stacking and preserving the phase purity of the as-grown rBN layers (Extended Data Fig. 1c).

Growth of single-crystal rBN film

To produce large-sized single-crystal rBN layers, a growth procedure with five typical stages was utilized (schematically illustrated in Fig. 1f). Specifically, the first 'substrate annealing' stage was set for preparing the large-sized single-crystal substrate of Ni(hk0) foil. The second 'surface reconstruction' stage was to form the parallel bunched steps with terrace Ni(100) and bevel Ni(110) on the as-prepared substrate. The third 'nucleation of rBN domains' stage was to enable the formation of unidirectionally aligned rBN domains with consistent ABC stacking (in addition, the diffusion of Ni atoms underneath the coverage of rBN layer will be greatly elevated in this stage, which could further augment the height of bunch steps and enlarge the area of bevel facets)[41,42]. The fourth special stage, called 'removing of the bunched steps', was added here to achieve a flat substrate by increasing the temperature close to the melting point of Ni, thereby facilitating the seamless stitching of rBN domains[35,43]. The final stage of 'growth of the uniform rBN multilayer film' was realized by long-term growth followed by subsequent etching (to eliminate the excessive layers at the top of rBN domains that have not yet stitched into an intact film) in our approach.

We experimentally prepared a substrate of single-crystal Ni(520) foil with a typical size of 4 × 4 cm^2 using the seeded growth method (Fig. 2a). X-ray diffraction (XRD) 2θ-scan patterns (Fig. 2b), reconstructed single-crystal XRD data (inset of Fig. 2b), and electron backscatter diffraction (EBSD) mappings (Fig. 2c,d and Extended Data Fig. 2) revealed the single crystallinity of the as-prepared substrate. After the surface reconstruction stage, the morphology of the bunched steps composed of terrace Ni(100) and bevel Ni(110) could be observed through atomic force microscopy (AFM) measurements, as the angles between two facets appeared to be approximately 135° based on statistics over a large area (Fig. 2e,f). Then a multilayer triangular domain with consistent orientation in each layer was found to be guided by such a bunched step in the nucleation stage (Fig. 2g), and the untwisted stacking of this domain was verified by a polarization-dependent second-harmonic generation (SHG) pattern with six-fold symmetry and coherently enhanced intensity (Fig. 2h). We further carried out atomically resolved measurements of planar and cross-sectional high-angle annular dark field (HAADF) scanning transmission electron microscopy (STEM) to definitively show the ABC stacking of the rBN phase (Fig. 2i,j and Extended Data Fig. 3a,b). We found that the rBN layers in close proximity to the Ni substrate surface showed a fast propagation rate at high growth temperature, to prevent the excessive dissolution of B into the Ni substrate that could form the alloy and thereby destroy the surface morphology of the bevel edges (Extended Data Fig. 3c–g). In contrast, without the guidance of bunched steps, the stacking order of the as-grown BN layers tends to be the AA′A type of the hBN phase (Extended Data Fig. 4). Therefore, we conclude that precise control from these bevel step edges leads to the formation of rBN domains.

These rBN domains were found to be unidirectionally aligned over a large area (Fig. 3a and Extended Data Fig. 5). To facilitate the growth and stitching of these rBN domains, a special stage, called 'removing of the bunched steps' with annealing at a temperature close to the melting point of Ni, was utilized to melt the morphology of the substrate from bunched steps into a flat surface, on which a layer-by-layer growth and stitching mode in these rBN domains could be realized (Fig. 3b). Atomically resolved STEM images were also collected around the concave corner in the joint area of two unidirectionally aligned rBN multilayer and bilayer domains, and the completely identical lattices

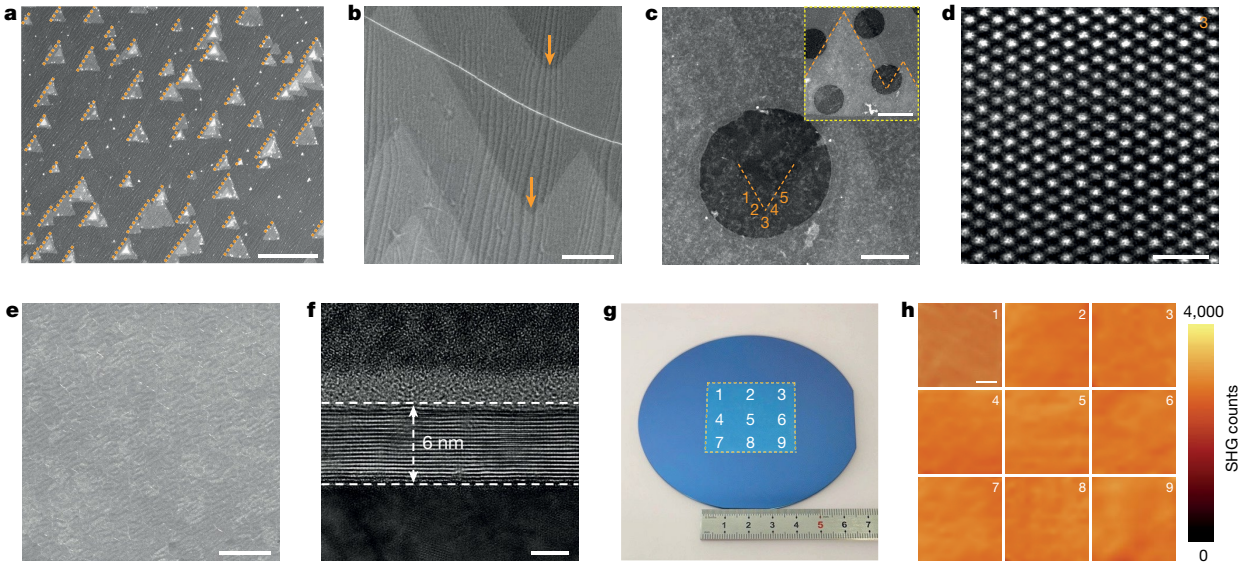

Fig. 3 | Seamless stitching of rBN domains into a uniform single-crystal multilayer film. a,**b**, SEM images of unidirectionally aligned rBN domains grown on single-crystal Ni foil (**a**) and the joint area of two aligned rBN domains (**b**), where the orange arrows shown in **b** indicate the layer-by-layer stitching mode in rBN domains through the SEM contrast. **c**, Low-magnification ADF-STEM image obtained at the concave corner in the joint area of the two aligned thick-layer rBN domains. Inset: zoom-out image of the stitched rBN domains with triangle contours. The edges of two rBN thick layers are marked by the dashed orange lines. **d**, Representative HAADF-STEM image collected at zone 3 marked in **c**, showing the uniform lattice of stitched thick-layer rBN domains without line defects. **e**, Typical SEM image of a continuous rBN film grown on the single-crystal Ni foil. **f**, Cross-sectional high-resolution transmission electron microscopy (HRTEM) image of the as-grown rBN film with a typical thickness of 6 nm. The zone axis is randomly selected here for determining the thickness of the as-grown rBN continuous film. **g**, Photograph of a 4 × 4-cm^2 rBN single-crystal film transferred onto a SiO_2/Si wafer with homogeneous optical contrast. **h**, SHG mappings of rBN collected at the corresponding areas marked in **g**, indicating the uniform thickness of the as-prepared rBN film. All images in **h** are the same size. Scale bars, 20 μm (**a**,**e**), 1 μm (**b**, inset in **c**), 0.3 μm (**c**), 0.5 nm (**d**), 3 nm (**f**), 5 μm (**h**).

verified the seamless stitching behaviour without grain boundaries (Fig. 3c,d and Extended Data Fig. 6). Through long-term growth at high temperature followed by subsequent etching (see details in Methods), single-crystal rBN film with thickness in the range of 2.2–12 nm was attained (Extended Data Fig. 7a). The statistics of the domain sizes at the nucleation stage and film thickness at the growth stage showed the appropriate growth rate of rBN layers under our growth conditions (Extended Data Fig. 7b,c), thereby ensuring high uniformity and quality of the as-grown continuous film. Experimentally, in a 4 × 4-cm^2 single-crystal rBN film with typical thickness of 6 nm (Fig. 3e–g), the uniformity over a wide range was determined by SHG mappings collected in 9 representative areas (Fig. 3h), as the SHG intensity shows a quadratic dependence on the number of rBN layers in our thickness range. Furthermore, the single-crystal nature as well as the high quality of the as-grown rBN layers was verified through combined characterizations of low-energy electron diffraction (LEED), ultraviolet–visible absorption spectroscopy (UV-vis), Raman spectroscopy and X-ray photoelectron spectroscopy (XPS) (Extended Data Fig. 7d–h). In addition, through the in situ comparison of SHG mappings before and after an additional etching process (Extended Data Fig. 7i,j), we found that the etching immediately after growth eliminated the unstitched excess layers, without compromising the surface quality of the as-grown rBN film.

Sliding ferroelectricity of rBN layers

The non-centrosymmetry in the out-of-plane direction of ABC-stacked rBN layers resulted in accumulative charge displacement and spontaneous electric polarization at the interface, which leads to interlayer sliding ferroelectricity. This hypothesis was verified through the theoretical simulation of the interlayer differential charge density of rBN and the corresponding line profile (Fig. 4a,b). To experimentally demonstrate the superiorities of interlayer sliding ferroelectricity in rBN layers, we performed piezo-response force microscopy (PFM) measurements on our as-grown samples. The similar hysteresis loops of phase and butterfly loops of amplitude collected on a special sample with continuous layer variation (which is 8, 9 and 10 layers in actuality; Fig. 4c,d) suggested robust interlayer ferroelectricity in rBN layers without the odd–even layer effect, frequently seen in the ABA-stacked BN layers, owing to that the ferroelectric dipole signs were opposite between the adjacent layers. It is generally known that accumulation of polarization with the number of layers is an important feature of 2D ferroelectric materials[18,19]. We also conducted in situ Kelvin probe force microscopy (KPFM) combined with an AFM scan at the region with the continuous layer variation in a rBN pyramidal domain transferred onto the wafer (gold-coated silicon dioxide (SiO_2)/silicon (Si)), and found that the surface potential of rBN increases with the number of layers, illustrating the sharp steps and an increment of approximately 60 mV per layer (Fig. 4e,f). Such a value is consistent with the one measured between opposite AB- and BA-stacked domains in a nearly parallel bilayer hBN film within first-harmonic KPFM[9], revealing the intrinsically accumulable polarization as well as the high quality of the rBN layers without vacancy and doping.

Furthermore, through in situ KPFM combined with conductive AFM measurements, the safe thickness of rBN layers was found to be 2 nm (Fig. 4g–i), indicating that rBN layers thicker than 2 nm could prevent ferroelectric failure caused by soft breakdown under the regular operating voltage of devices. We further investigated the evolution of PFM responses under different alternating-current (a.c.) and direct-current (d.c.) biases and confirmed that the ferroelectric signals were intrinsic rather than extrinsic artefacts such as ion migration (Extended Data Fig. 8a,b). In addition, a significant and clear ferroelectric response could be still observed at 450 K (Fig. 4j), indicating a high Curie temperature of the rBN layers. Besides, reproducibility of the ferroelectricity in rBN layers was demonstrated through the typical and similar ferroelectric characteristics measured on nine samples, which were

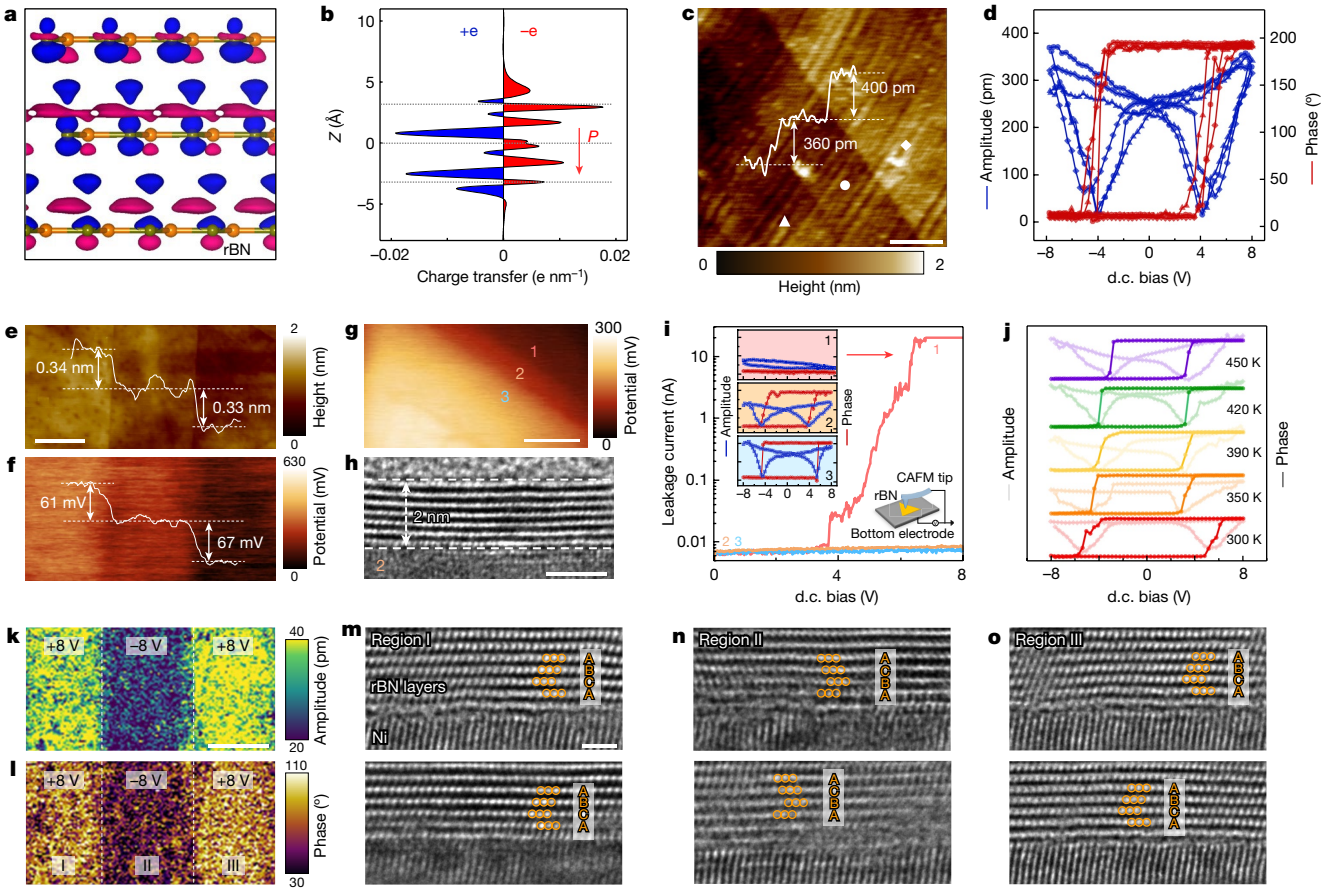

Fig. 4 | The interfacial sliding ferroelectricity in rBN layers. a,**b**, Interlayer differential charge density (**a**) and the corresponding line profiles (**b**) of rBN layers, where *Z* is the position along the *Z* direction and *P* is the polarization. **c**, AFM topographic image of a special area with continuous layer variation in the rBN film (8, 9 and 10 layers, respectively), where the overlaid curve is the corresponding height profile, and three white symbols were used to indicate different layers in this sample. **d**, PFM measurements on each rBN layer marked in **c**. The blue and red data correspond to the amplitude and phase results, respectively. **e**,**f**, AFM height mapping (**e**) and the corresponding KPFM measurement (**f**) collected on the rBN area with consecutive layer variation, indicating the surface potential of rBN is linearly dependent on its layer number. **g**–**i**, Combined ferroelectric failure test by KPFM mapping (**g**), a cross-sectional HRTEM image (**h**) and the bias-dependent leakage current curves (**i**). The HRTEM image (**h**) showing the safe thickness of about 2 nm was collected at zone 2 marked in **g**. The zone axis of **h** was randomly selected. The current–bias curves (**i**) and corresponding PFM signals (left insets) measured at zones 1, 2 and 3 (with a thickness of 6, 7 and 9 layers, respectively) were shown in **g**, indicating that a large leakage current leads to ferroelectric failure. The bottom right inset of **i** is the schematic illustration of the CAFM setup. **j**, Temperature-dependent PFM signals of a 19-layer rBN film, suggesting a high ferroelectric Curie temperature greater than 450 K. **k**,**l**, PFM amplitude (**k**) and phase (**l**) images of the same area of multilayer rBN film. **m**–**o**, Two typical cross-sectional HRTEM images taken in regions I (**m**), II (**n**) and III (**o**) marked in **l**, respectively. The zone axes are the zigzag direction of the rBN layers. All images in **m**–**o** are the same size. With the reference of Ni lattice shown in the images, a change of the stacking order of the rBN sample can be clearly seen from ABC (region I and III) to CBA (region II). In this figure, the hysteresis and butterfly loops are the phase and amplitude results, respectively. Scale bars, 200 nm (**c**), 500 nm (**e**), 5 μm (**g**), 2 nm (**h**), 500 nm (**k**), 1 nm (**m**).

grown using the same approach but in different batches (Extended Data Fig. 8c). As a control, we also carried out similar theoretical simulations and experimental measurements on hBN layers with centrosymmetric AA′A stacking, but no ferroelectric response could be found or detected (Extended Data Fig. 9).

One promising application of 2D ferroelectricity widely discussed is non-volatile data storage, which has advantages, such as fast reading and writing speed, low energy consumption, remarkable endurance and so on, over traditional magnetic-based memories, and manipulation of the rBN ferroelectric domain is an essential prerequisite to realize these applications[44–46]. However, a critical issue is whether ferroelectric switching can be achieved through interlayer slidings in epitaxially grown rBN layers. As shown in Fig. 4k,l, an area of multilayer rBN film on single-crystal Ni foil was initially poled with a d.c. bias of +8 V; then only the middle region was reversely poled with an opposite d.c. bias of −8 V. Thereby, three regions (I, II and III) with opposite polarization were created. The cross-sectional STEM images taken at these regions demonstrate the switching of polarization corresponding to a change of the stacking order in the rBN sample from ABC stacking to CBA stacking (Fig. 4m–o). In particular, the clear and consistent Ni lattices across all regions establish a reference for such ABC and CBA stacking within one rBN film.

In principle, the sliding process necessitates overcoming a specific energy barrier compared with relatively stable states before and after switching. Through the theoretical investigations, we found that: (1) the energy barriers for sliding to the opposite stacking configuration along the optimal pathway are in the range of a few millielectronvolts (meV) per atom (Extended Data Fig. 10a–c); (2) the formation energy of a domain wall with a width of approximately 10 nm is at the level of several meV per atom (Extended Data Fig. 10d–f); (3) nucleation of a new domain needs to surmount a slightly larger barrier of approximately 10 meV per atom, which shows a downwards trend with propagation of the nucleus (Extended Data Fig. 10g). All these results corroborate the feasibility of polarization switching and the domain manipulation

in rBN layers, as long as a sufficient external driving force could be provided.

Summary

We have reported a facile methodology for bevel-edge epitaxy of 2D layers with effective control over both the lattice orientation of each layer and the sliding vector at every interface. On a substrate with a parallel step bunching morphology consisting of terrace Ni(100) and bevel Ni(110), a 4 × 4-cm^2 single-crystal rBN film with uniform thickness in the range of 2.2–12 nm was grown. Then, robust, homogeneous and switchable ferroelectricity with a high Curie temperature was demonstrated in the as-grown rBN layers, which holds great promise for realizing advanced devices based on multifunctional 2D dielectric materials.

Online content

Any methods, additional references, Nature Portfolio reporting summaries, source data, extended data, supplementary information, acknowledgements, peer review information; details of author contributions and competing interests; and statements of data and code availability are available at https://doi.org/10.1038/s41586-024-07286-3.

1. Dean, C. R. et al. Boron nitride substrates for high-quality graphene electronics. *Nat. Nanotechnol.* **5**, 722–726 (2010).
2. Liu, Z. et al. Ultrathin high-temperature oxidation-resistant coatings of hexagonal boron nitride. *Nat. Commun.* **4**, 2541 (2013).
3. Cassabois, G., Valvin, P. & Gil, B. Hexagonal boron nitride is an indirect bandgap semiconductor. *Nat. Photon.* **10**, 262–266 (2016).
4. Zhu, K. et al. Hybrid 2D-CMOS microchips for memristive applications. *Nature* **618**, 57–62 (2023).
5. Li, Y. L. et al. Probing symmetry properties of few-layer MoS_2 and h-BN by optical second-harmonic generation. *Nano Lett.* **13**, 3329–3333 (2013).
6. Kim, C. J. et al. Stacking order dependent second harmonic generation and topological defects in h-BN bilayers. *Nano Lett.* **13**, 5660–5665 (2013).
7. Li, L. & Wu, M. Binary compound bilayer and multilayer with vertical polarizations: two-dimensional ferroelectrics, multiferroics, and nanogenerators. *ACS Nano* **11**, 6382–6388 (2017).
8. Yasuda, K., Wang, X., Watanabe, K., Taniguchi, T. & Jarillo-Herrero, P. Stacking-engineered ferroelectricity in bilayer boron nitride. *Science* **372**, 1458–1462 (2021).
9. Vizner Stern, M. et al. Interfacial ferroelectricity by van der Waals sliding. *Science* **372**, 1462–1466 (2021).
10. Woods, C. et al. Charge-polarized interfacial superlattices in marginally twisted hexagonal boron nitride. *Nat. Commun.* **12**, 347 (2021).
11. Lv, M. et al. Spatially resolved polarization manipulation of ferroelectricity in twisted hBN. *Adv. Mater.* **34**, 2203990 (2022).
12. Qi, J. et al. Stacking-controlled growth of rBN crystalline films with high nonlinear optical conversion efficiency up to 1%. *Adv. Mater.* **36**, 2303122 (2023).
13. Fei, Z. et al. Ferroelectric switching of a two-dimensional metal. *Nature* **560**, 336–339 (2018).
14. Xiao, J. et al. Intrinsic two-dimensional ferroelectricity with dipole locking. *Phys. Rev. Lett.* **120**, 227601 (2018).
15. Weston, A. et al. Interfacial ferroelectricity in marginally twisted 2D semiconductors. *Nat. Nanotechnol.* **17**, 390–395 (2022).
16. Wang, X. et al. Interfacial ferroelectricity in rhombohedral-stacked bilayer transition metal dichalcogenides. *Nat. Nanotechnol.* **17**, 367–371 (2022).
17. Rogee, L. et al. Ferroelectricity in untwisted heterobilayers of transition metal dichalcogenides. *Science* **376**, 973–978 (2022).
18. Deb, S. et al. Cumulative polarization in conductive interfacial ferroelectrics. *Nature* **612**, 465–469 (2022).
19. Meng, P. et al. Sliding induced multiple polarization states in two-dimensional ferroelectrics. *Nat. Commun.* **13**, 7696 (2022).
20. Jindal, A. et al. Coupled ferroelectricity and superconductivity in bilayer T_d-$MoTe_2$. *Nature* **613**, 48–52 (2023).
21. Ko, K. et al. Operando electron microscopy investigation of polar domain dynamics in twisted van der Waals homobilayers. *Nat. Mater.* **22**, 992–998 (2023).
22. Zhang, D., Schoenherr, P., Sharma, P. & Seidel, J. Ferroelectric order in van der Waals layered materials. *Nat. Rev. Mater.* **8**, 25–40 (2023).
23. Wang, C., You, L., Cobden, D. & Wang, J. Towards two-dimensional van der Waals ferroelectrics. *Nat. Mater.* **22**, 542–552 (2023).
24. Chubarov, M., Pedersen, H., Högberg, H., Jensen, J. & Henry, A. Growth of high quality epitaxial rhombohedral boron nitride. *Cryst. Growth Des.* **12**, 3215–3220 (2012).
25. Sutter, P., Lahiri, J., Zahl, P., Wang, B. & Sutter, E. Scalable synthesis of uniform few-layer hexagonal boron nitride dielectric films. *Nano Lett.* **13**, 276–281 (2013).
26. Gilbert, S. M. et al. Alternative stacking sequences in hexagonal boron nitride. *2D Mater.* **6**, 021006 (2019).
27. Lu, J. et al. Step flow versus mosaic film growth in hexagonal boron nitride. *J. Am. Chem. Soc.* **135**, 2368–2373 (2013).
28. Zhang, C. H. et al. Controllable co-segregation synthesis of wafer-scale hexagonal boron nitride thin films. *Adv. Mater.* **26**, 1776–1781 (2014).
29. Wang, L. F. et al. Monolayer hexagonal boron nitride films with large domain size and clean interface for enhancing the mobility of graphene-based field-effect transistors. *Adv. Mater.* **26**, 1559–1564 (2014).
30. Kim, S. M. et al. Synthesis of large-area multilayer hexagonal boron nitride for high material performance. *Nat. Commun.* **6**, 8662 (2015).
31. Lee, J. S. et al. Wafer-scale single-crystal hexagonal boron nitride film via self-collimated grain formation. *Science* **362**, 817–821 (2018).
32. Wang, L. et al. Epitaxial growth of a 100-square-centimetre single-crystal hexagonal boron nitride monolayer on copper. *Nature* **570**, 91–95 (2019).
33. Chen, T. A. et al. Wafer-scale single-crystal hexagonal boron nitride monolayers on Cu (111). *Nature* **579**, 219–223 (2020).
34. Shi, Z. Y. et al. Vapor-liquid-solid growth of large-area multilayer hexagonal boron nitride on dielectric substrates. *Nat. Commun.* **11**, 849 (2020).
35. Ma, K. Y. et al. Epitaxial single-crystal hexagonal boron nitride multilayers on Ni (111). *Nature* **606**, 88–93 (2022).
36. Fukamachi, S. et al. Large-area synthesis and transfer of multilayer hexagonal boron nitride for enhanced graphene device arrays. *Nat. Electron.* **6**, 126–136 (2023).
37. Jang, A.-R. et al. Wafer-scale and wrinkle-free epitaxial growth of single-orientated multilayer hexagonal boron nitride on sapphire. *Nano Lett.* **16**, 3360–3366 (2016).
38. Cazorla, C. & Gould, T. Polymorphism of bulk boron nitride. *Sci. Adv.* **5**, eaau5832 (2019).
39. Kubota, Y., Watanabe, K., Tsuda, O. & Taniguchi, T. Deep ultraviolet light-emitting hexagonal boron nitride synthesized at atmospheric pressure. *Science* **317**, 932–934 (2007).
40. Li, J. et al. Hexagonal boron nitride crystal growth from iron, a single component flux. *ACS Nano* **15**, 7032–7039 (2021).
41. Yi, D. et al. What drives metal-surface step bunching in graphene chemical vapor deposition? *Phys. Rev. Lett.* **120**, 246101 (2018).
42. Gunther, S. et al. Single terrace growth of graphene on a metal surface. *Nano Lett.* **11**, 1895–1900 (2011).
43. Wang, Z.-J. et al. The coalescence behavior of two-dimensional materials revealed by multiscale in situ imaging during chemical vapor deposition growth. *ACS Nano* **14**, 1902–1918 (2020).
44. Wu, G. et al. Programmable transition metal dichalcogenide homojunctions controlled by nonvolatile ferroelectric domains. *Nat. Electron.* **3**, 43–50 (2020).
45. Wang, S. et al. Two-dimensional ferroelectric channel transistors integrating ultra-fast memory and neural computing. *Nat. Commun.* **12**, 53 (2021).
46. Wang, X. et al. Van der Waals engineering of ferroelectric heterostructures for long-retention memory. *Nat. Commun.* **12**, 1109 (2021).

Methods

Annealing of single-crystal Ni(520) foils

A commercial polycrystalline Ni foil (100-μm thick, 99.994%, Zhongke Crystal Materials) was placed on an aluminium oxide (Al_2O_3) plate and loaded into a tube furnace with a chamber diameter of 6 cm (Hefei Kejing). Using the seeded growth method[47], the foil was annealed at 1,410 °C for 10 h in a reducing atmosphere (500 standard cubic centimetres per minute (sccm) argon and 50 sccm hydrogen) to obtain the single-crystal Ni(520) foil. After that, the whole system was naturally cooled to room temperature with a fixed gas flow.

Growth of single-crystal rBN multilayer films

The precursor ammonia borane (97%, Aldrich) was added to an Al_2O_3 crucible and placed 1 m upstream from the single-crystal Ni(520) substrate. As shown in +. 1f, the foil was heated to 1,410 °C with a reducing flux (500 sccm argon and 50 sccm hydrogen) and kept at this temperature for 30 min to remove the surface impurities and oxides at atmospheric pressure. Then the temperature was decreased to 1,350 °C and the Ni foil was annealed at this temperature for 3 h to form the parallel bunched steps. For the subsequent nucleation and growth of rBN multilayers, the system was switched to low pressure with argon (70 sccm) and hydrogen (30 sccm) and the precursor was heated to 65 °C within 10 min using a heating band. The furnace was fixed at 1,350 °C for 1 h to nucleate the unidirectional rBN domains, then re-heated to 1,410 °C and kept at this temperature for 2–10 h to grow aligned domains as well as continuous films with different thickness. To obtain more uniform rBN films, the system was finally switched to atmospheric pressure with argon (400 sccm) and hydrogen (100 sccm) and kept at 1,410 °C for 10 min to etch the excess layers at the top of the rBN domains that had not yet stitched into an intact film. After that, the furnace was naturally cooled to room temperature with argon (500 sccm) and hydrogen (10 sccm).

Transfer of rBN single crystals

A polypropylene carbonate (PPC)-assisted wet-transfer method was used to transfer rBN domains and films. First, the rBN/Ni samples were spin-coated with a PPC film, and then floated on the surface of 0.1 mol L^{-1} iron chloride ($FeCl_3$) solution to remove the Ni substrates. Subsequently, the PPC-coated rBN samples were rinsed with deionized water several times and placed onto the target substrates, including SiO_2/Si wafers, gold-coated SiO_2/Si wafers and holey-carbon-film transmission electron microscopy (TEM) grids (Zhongjingkeyi GIG-1213-3C). Finally, the sample and substrate systems were loaded into a clean tube in a chemical vapour deposition system, and annealed at low pressure (about 200 Pa) and a suitable temperature (500 °C for SiO_2/Si wafers and 300 °C for TEM grids) for 10 h with a fixed gas flow (500 sccm argon and 10 sccm hydrogen) to remove the residual PPC films.

AFM measurements

The topographic mappings of bunched steps on the Ni surface and the transferred BN multilayers were obtained by a Bruker Dimensional ICON system, and the other room-temperature measurements were performed on an Asylum Research MFP-3D atomic force microscope. An Asylum Research Cypher ES atomic force microscope with environmental control was used for single-pass KPFM and temperature-dependent PFM measurements. Conductive platinum-coated probes with a radius of <40 nm, a spring constant of about 2 N m^{-1} and a mechanical resonance frequency of about 75 kHz were used in all-electrical AFM modules. Conductive AFM was performed in an ORCA module with a compliance current of 20 nA. In the KPFM measurements, the lift height of the probe was 20–50 nm for the double-pass mode. The electrical drive amplitude was set to 3 V, the electrical frequency was 5 kHz and all KPFM images were scanned in attractive mode to minimize the crosstalk of height and potential signals. Data analysis was performed using Asylum Research official software.

For a typical switching spectroscopy PFM measurement, an a.c. voltage (V_{ac}, sin wave) was carried by a d.c. voltage (V_{dc}, square wave) that stepped over time, both of which were applied on the tip. Between each voltage step, V_{dc} returned to zero (off mode) while V_{ac} was still applied to test the ferroelectric response. To effectively weaken the contribution of ion motion and charge effect[48–51], here we show all PFM hysteresis loops in off mode. For PFM mappings, only an appropriate amount of V_{ac} was applied and V_{dc} was set to zero. In our cases, after writing the arbitrary ferroelectric domain structures with a strong V_{dc}, V_{ac} = 1 V was applied to read them. Temperature-dependent PFM was performed on a ceramic heating plate under a nitrogen atmosphere.

TEM characterizations

For cross-sectional TEM and STEM characterizations, a dual-beam focused ion beam (FIB) system (Thermo Scientific Scios 2) was used for preparing the samples[52]. A 200-nm protective layer made of carbon was first deposited using FIB e-beam deposition. After tilting the sample by 52° with respect to the ion beam, a tungsten strap layer of 1 μm was then deposited to protect the region of interest during milling. A 30-kV Ga^+ beam with a current of 0.1–1 nA was used to reduce the specimen thickness to 50–100 nm for further characterizations. For in-plane TEM and STEM characterizations, samples were wet-transferred onto the TEM grids and the experiments were performed in a JEOL JEM-ARM300F operated at 300 kV. For STEM imaging, the electron beam was converged to <0.1 nm with a semi-convergence angle of about 22 mrad with a 30-μm condenser lens aperture to scan the sample. The collection angles of HAADF-STEM images were set as about 60–230 mrad. All data were collected and analysed using Digital Micrograph.

Other characterizations

Scanning electron microscopy (SEM) images were collected by a Hitachi SU-8220 scanning electron microscope. EBSD was performed using a PHI 710 scanning Auger nanoprobe. LEED patterns were obtained by a LEED-Auger spectrometer BDL800IR system in ultrahigh vacuum with a base pressure below 3×10^{-7} Pa. XRD 2θ-scan data were obtained using a Bruker D8 Advance system with a silver target, and single-crystal XRD measurements were performed using a Bruker D8 Venture system. SHG measurements were conducted by WiTec alpha300R with an incident light wavelength of 1,064 nm, a fixed excitation power of 20 mW and an integration time of 0.2 s. The Raman spectrum was obtained at room temperature using a SmartRaman confocal-micro-Raman module (Institute of Semiconductors, Chinese Academy of Sciences) with an incident light wavelength of 532 nm. XPS and ultraviolet–visible spectra were performed using an Axis Ultra Imaging X-ray photoelectron spectrometer and a Varian Cary 5000 ultraviolet–visible-NIR spectrophotometer, respectively.

Computational details

Geometric optimization and energy calculations of the BN/Ni systems were carried out using density functional theory (DFT) as implemented in Vienna Ab-initio Simulation Package (VASP 5.4.4)[53,54]. The exchange-correlation functions were treated by the generalized gradient approximation and the interaction between valence electrons and ion cores was carried out by the projected-augmented-wave method[55,56]. The plane-wave cut-off energy was set at 400 eV for the BN/Ni systems and 600 eV for BN multilayers. The dispersion-corrected DFT-D3 method was used because of its good description of long-range van der Waals interactions for multilayer two-dimensional materials. The geometries of the BN/Ni systems were relaxed until the force on each atom was less than 0.02 eV $Å^{-1}$ and the energy convergence criterion of 1×10^{-4} eV was met. The Ni surfaces were modelled by a periodic slab and some bottom layers were fixed to mimic the bulk, where a 1 × 1 × 1 Monkhorst–Pack k-point mesh was adopted. The binding energy of the Ni–BN hybrid, namely, $E_b = (E_{total} - E_{BN} - E_{sub})/l$, was

calculated using the relaxed structures, where E_{total} is the total energy of the system, E_{BN} and E_{sub} represent the energies of BN and the substrate, respectively, and l is the length along the step. The Berry-phase method was used to evaluate crystalline polarization for BN multilayers[57], and the nudged-elastic-band method was used to calculate the ferroelectric switch pathway[58], where the Brillouin zone was sampled with $25 \times 25 \times 1$ k-points for structural relaxation and $12 \times 12 \times 1$ k-points for the calculation of the ferroelectric switch pathway, while the forces on all atoms were optimized to be less than 0.005 eV Å^{-1} and the tolerance for the energy convergence was set to 10^{-6} eV. The van der Waals correction of the Becke–Johnson damping function is applied, and the vacuum space is set to 40 Å to avoid the interaction from the layers of adjacent unit cells.

To obtain the transition energy barrier for nucleating the multilayer rBN domain from ABC to CBA stacking, force-field calculations were performed by using the Large-scale Atomic/Molecular Massively Parallel Simulator (LAMMPS)[59]. The interactions in layered rBN systems were described by the registry-dependent interlayer potential and the Kolmogorov Crespi potential[60]. A three-layered rBN model with a size of 32.3×32.3 nm^2 was first constructed, featuring an ABC-stacking sequence. Subsequently, a CBA-stacking nucleus with a radius (r) of 1.0 nm, 1.5 nm, 2.0 nm, 2.5 nm, 3.0 nm and 3.5 nm was created at the centre of the model, and the width of domain boundary between ABC and CBA stacking was kept a constant value of 5 nm. After that, the relaxation of the generated models was performed by the conjugate gradient algorithms with a step of 100,000, where the CBA-stacking region was fixed while other parts were relaxed. As a result, the ABC stacking was totally transited into CBA stacking when r was greater than 3.0 nm. The energy barrier for the transition of the rBN layers from ABC to CBA stacking was calculated to be about 10 meV per atom, which was defined by dividing the energy barrier by the total number of atoms in the CBA stacking and the domain boundary region. Experimentally, the driving force is sufficient enough to overcome the calculated energy barrier for the transition from ABC to CBA stacking.

Data availability

The data that support the findings of this study are available within the paper. Additional data are available from the corresponding authors upon request. Source data are provided with this paper.

47. Wu, M. H. et al. Seeded growth of large single-crystal copper foils with high-index facets. *Nature* **581**, 406–410 (2020).
48. Guan, Z. et al. Identifying intrinsic ferroelectricity of thin film with piezoresponse force microscopy. *AIP Adv.* **7**, 095116 (2017).
49. Wu, M. et al. Achieving ferroelectricity in a centrosymmetric high-performance semiconductor by strain engineering. *Adv. Mater.* **35**, 2300450 (2023).
50. Gruverman, A., Alexe, M. & Meier, D. Piezoresponse force microscopy and nanoferroic phenomena. *Nat. Commun.* **10**, 1661 (2019).
51. Shi, W. et al. Reversible writing of high-mobility and high-carrier-density doping patterns in two-dimensional van der Waals heterostructures. *Nat. Electron.* **3**, 99–105 (2020).
52. Haigh, S. J. et al. Cross-sectional imaging of individual layers and buried interfaces of graphene-based heterostructures and superlattices. *Nat. Mater.* **11**, 764–767 (2012).
53. Kresse, G. & Furthmüller, J. Efficiency of ab-initio total energy calculations for metals and semiconductors using a plane-wave basis set. *Comput. Mater. Sci.* **6**, 15–50 (1996).
54. Kresse, G. & Hafner, J. Ab initio molecular dynamics for open-shell transition metals. *Phys. Rev. B* **48**, 13115 (1993).
55. Perdew, J. P., Burke, K. & Ernzerhof, M. Generalized gradient approximation made simple. *Phys. Rev. Lett.* **77**, 3865 (1996).
56. Kresse, G. & Joubert, D. From ultrasoft pseudopotentials to the projector augmented-wave method. *Phys. Rev. B* **59**, 1758 (1999).
57. King-Smith, R. & Vanderbilt, D. Theory of polarization of crystalline solids. *Phys. Rev. B* **47**, 1651 (1993).
58. Henkelman, G., Uberuaga, B. P. & Jónsson, H. A climbing image nudged elastic band method for finding saddle points and minimum energy paths. *J. Chem. Phys.* **113**, 9901–9904 (2000).
59. Plimpton, S. Fast parallel algorithms for short-range molecular dynamics. *J. Comput. Phys.* **117**, 1–19 (1995).
60. Ouyang, W., Mandelli, D., Urbakh, M. & Hod, O. Nanoserpents: graphene nanoribbon motion on two-dimensional hexagonal materials. *Nano Lett.* **18**, 6009–6016 (2018).

Acknowledgements This work was supported by the National Natural Science Foundation of China (52025023, 51991344, 12334001, 51991342, 52021006, 52272173, 92163206, 11888101, T2188101, 12104018, 12104493, 52172035, 92163206 and 22333005), National Key R&D Program of China (2023YFB4603603, 2022YFA1403500 and 2021YFA1400502), Guangdong Major Project of Basic and Applied Basic Research (2021B0301030002), the Strategic Priority Research Program of Chinese Academy of Sciences (XDB33000000), the National Postdoctoral Program for Innovative Talents (BX20220117 and BX20230022), China Postdoctoral Science Foundation (2022M721224 and 2023M730103), and the New Cornerstone Science Foundation through the XPLORER PRIZE. L.W. thanks support from the Youth Innovation Promotion Association of CAS. W.W. thanks the National Supercomputer Centre in Tianjin for computing support.

Author contributions X.B., K.L. and L.W. supervised the project. L.W., K.L., X.B. and X.Z. conceived the project. L.W., K.L., F.D., X.Z. and E.W. developed the growth and ferroelectricity mechanism. X.B. and L.W. organized the structural characterization. L.W., J.Q., Z.Z., Muhong Wu, W. Wang and X.X. conducted the preparation of single-crystal Ni(520) foils and rBN multilayer films. W. Wei, C.Z., Y.S., Menghao Wu and F.D. performed the theoretical calculations. Mengqi Wu, J.Q. and X.Z. performed the scanning probe-based characterizations. X.L., H.S., Q.G., M.C., Z.L., L.W., P.G. and X.B. performed the STEM and TEM measurements. J.Q., Z.Z., Q.W., Z.X., C.L., H.H., Z.-J.W. and L.W. performed the SEM, EBSD, LEED, XRD, SHG, Raman, ultraviolet–visible and XPS experiments. All authors discussed the results and wrote the paper.

Competing interests The authors declare no competing interests.

Additional information

Correspondence and requests for materials should be addressed to Li Wang, Feng Ding, Xiaorui Zheng, Kaihui Liu or Xuedong Bai.

Peer review information *Nature* thanks Kenji Yasuda, Hyobin Yoo and the other, anonymous, reviewer(s) for their contribution to the peer review of this work.

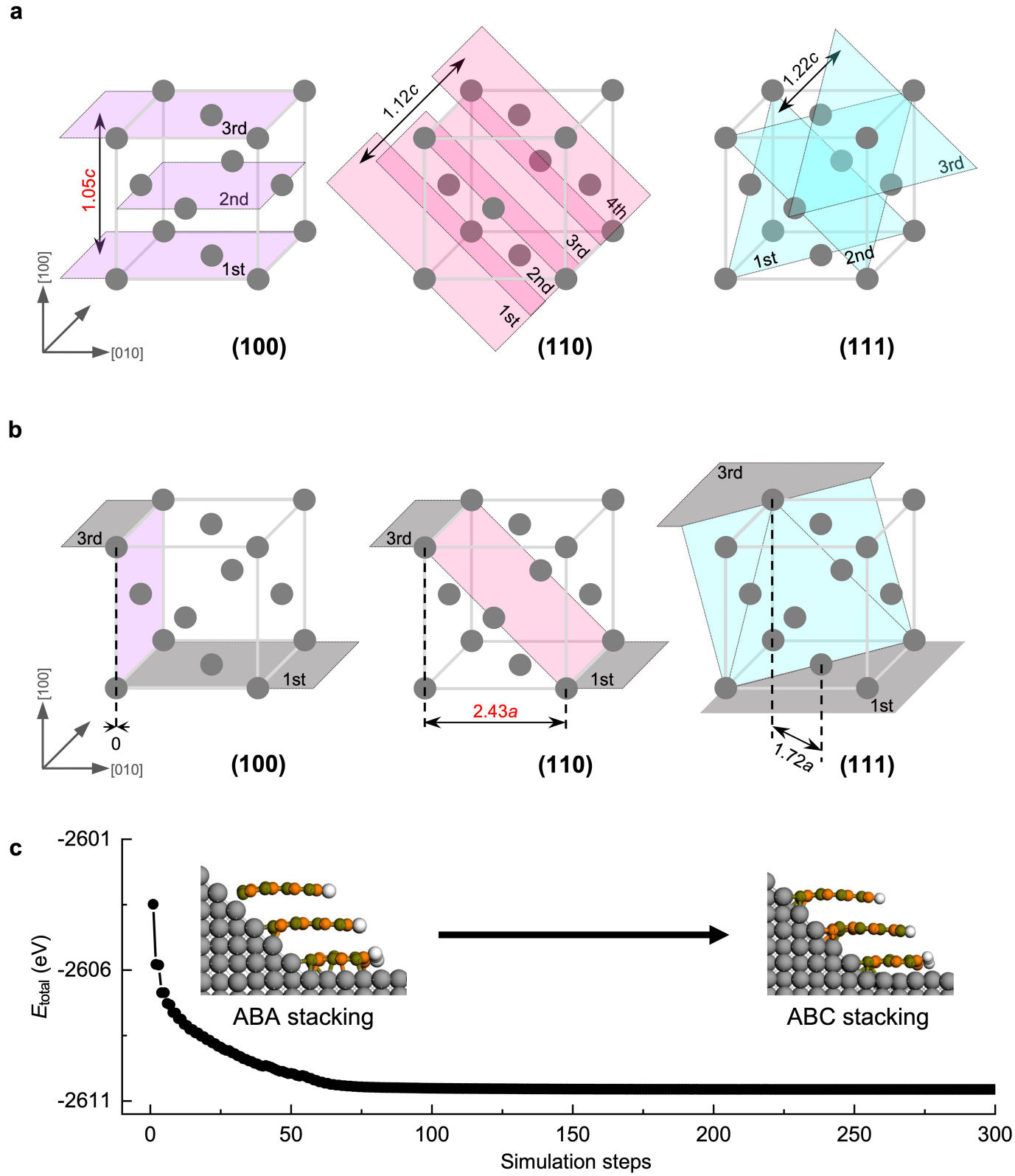

Extended Data Fig. 1 | Designing the most suitable terrace and bevel facets of bunched steps. a, Schematic illustrations of the interlayer spacing mismatch between the rBN and three low-index facets of Ni substrates, where the spacing distances of the (100), (110) and (111) facets are 1.05, 1.12 and 1.22 times the interlayer spacing of the rBN layers (*c*), respectively. **b**, Schematic illustrations of the interlayer sliding mismatch, where the horizontal distance of adjacent edges at the bevel facets of (100), (110) and (111) is 0, 2.43 and 1.72 times the single B-N bond length (*a*). Considering that the interlayer sliding in rBN layers is constant integer times of the half B-N bond length along the armchair direction, the (110) facet is chosen as the best bevel facet. **c**, Binding energy of unstable ABA-stacked hBN attached to the bevel facet of bunched steps, suggesting the spontaneous relaxation to ABC stacking. The orange, green, grey and white balls represent the B, N, Ni and H atoms, respectively.

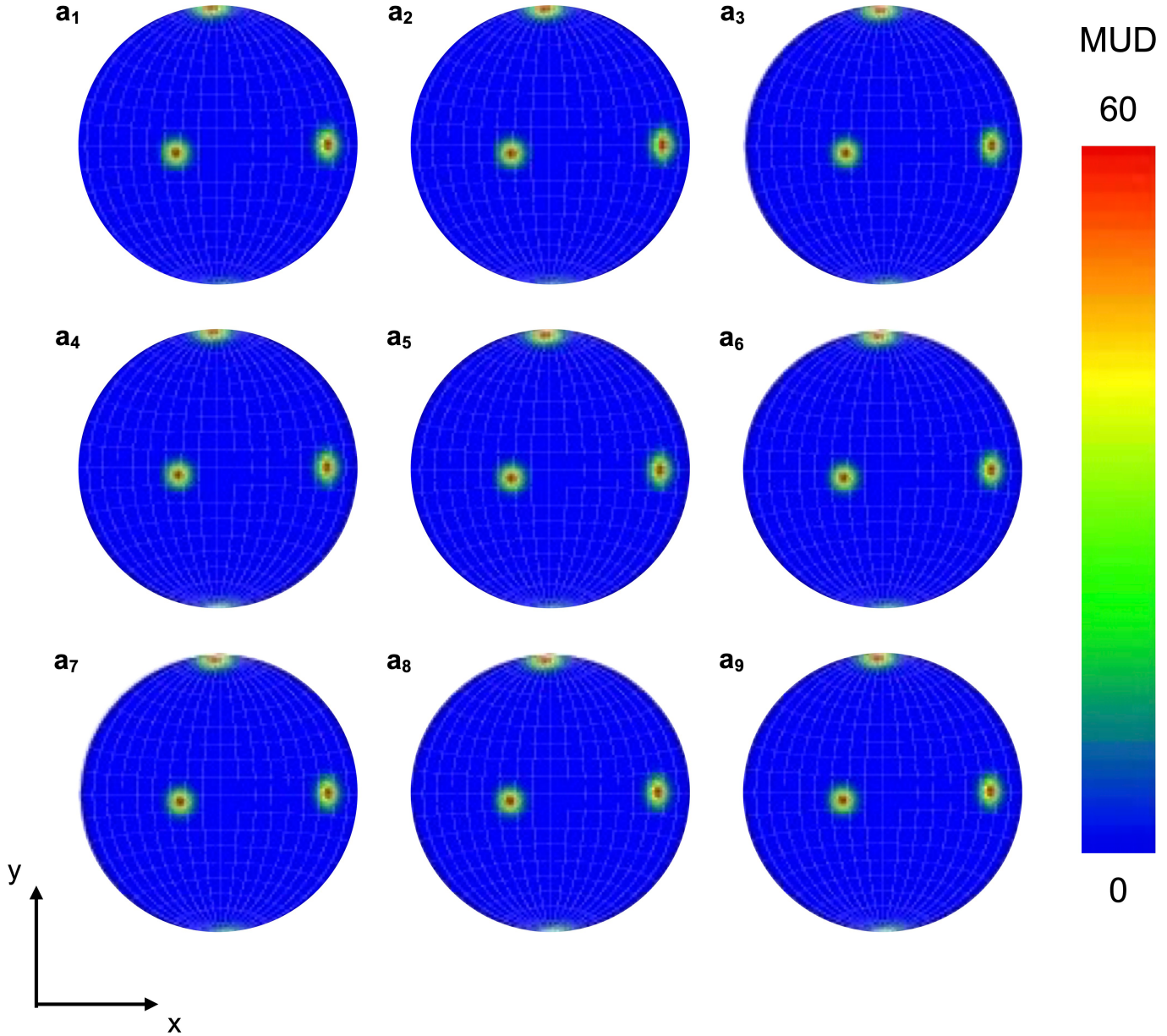

Extended Data Fig. 2 | EBSD pole figures of the single-crystal Ni(520) foil measured at different positions. The multiples of uniform density (MUD) results present the unidirectional orientation without in-plane rotation.

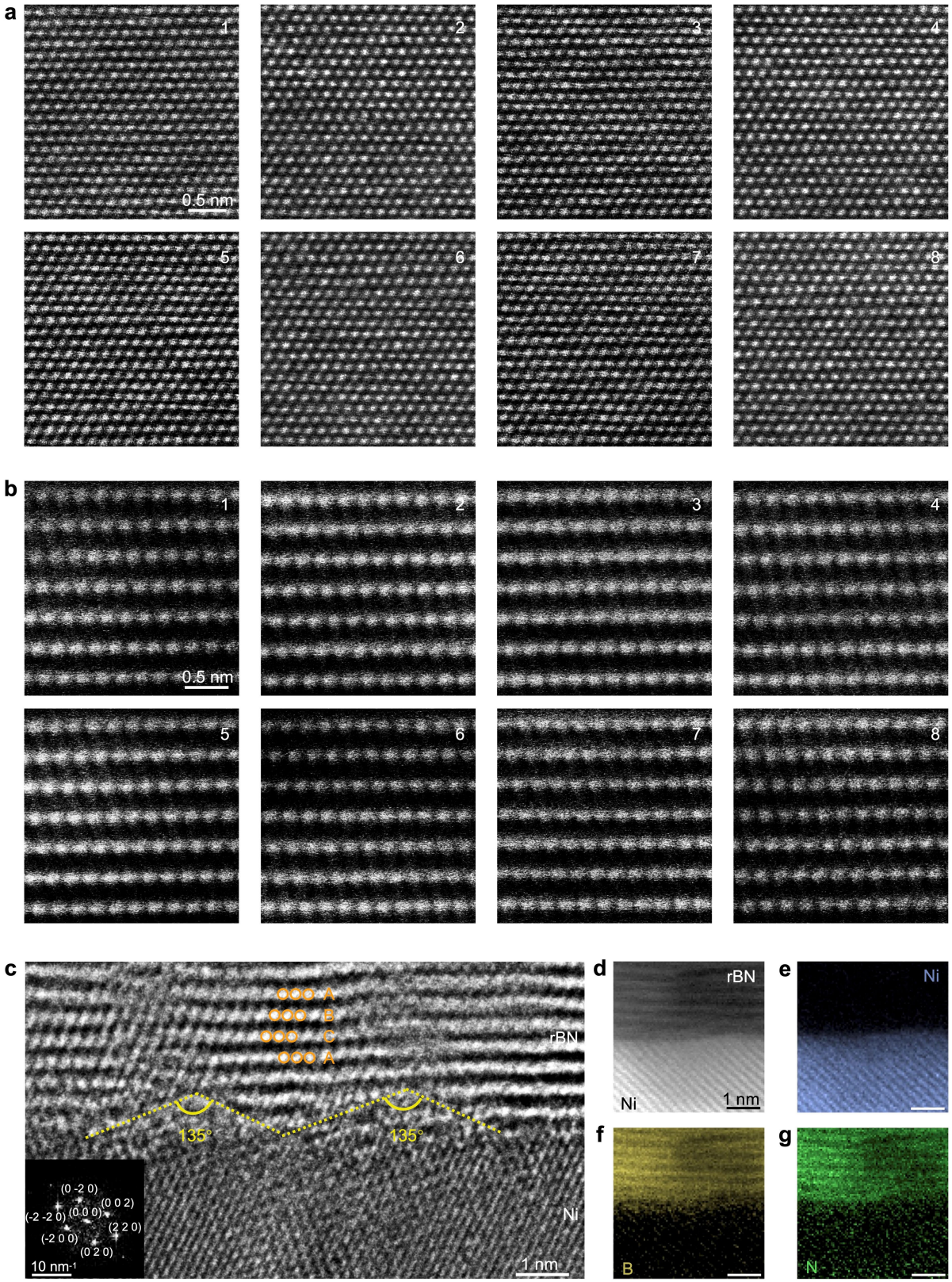

Extended Data Fig. 3 | Atomic configuration of rBN. a, Typical planar STEM images of rBN layers. All images are the same size. **b**, Typical cross-sectional STEM images of rBN layers with consistent ABC stacking. The zone axes are the zigzag direction of rBN layers here. All images are the same size. **c**, Representative cross-sectional HRTEM image of as-grown rBN layer on Ni(520) substrate. The bunched steps with angle of 135° on the Ni(520) surface are denoted with yellow dotted lines. Zone axis is zigzag direction of rBN layers here. **d**-**g**, Cross-sectional STEM image of rBN layers grown on Ni substrate (**d**), electron energy-loss spectroscopy (EELS) mappings of Ni (**e**), B (**f**) and N (**g**), implying the absence of Ni-B alloys at interface.

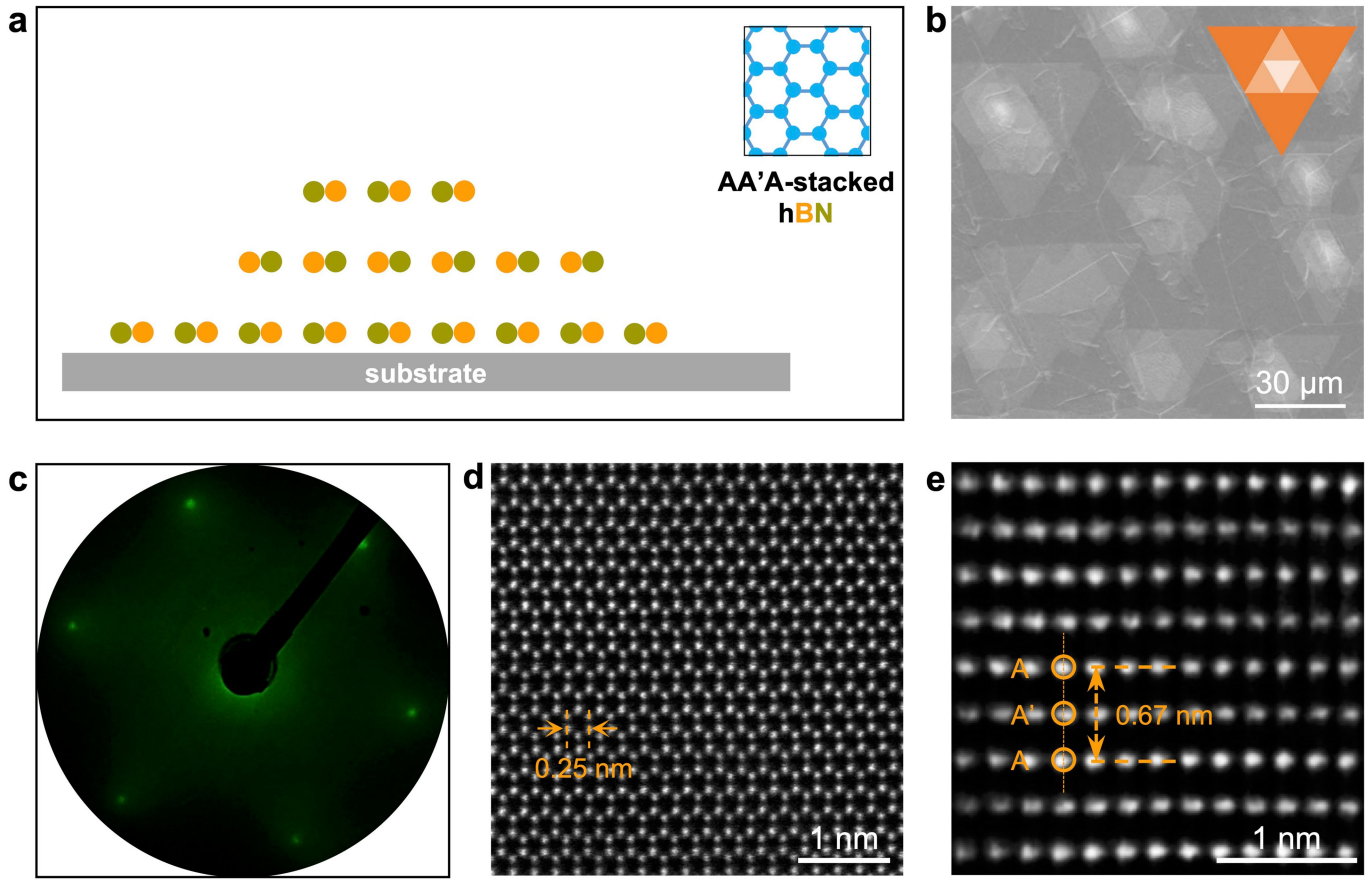

Extended Data Fig. 4 | Comparative results for growing AA'A-stacked hBN multilayers. a, Schematic illustration of the growth of inherently stable hBN multilayer domains on the Ni surface without guidance from bevel edges. Inset, top view of the AA'A-stacked hBN lattice. The orange, green and blue balls represent the B, N and overlapped B and N atoms, respectively. **b**, Typical SEM image of multilayer hBN domains with the typically opposite orientation in the adjacent layers grown on the Ni foil without bevel edges. Inset, scheme of the anti-parallelly stacked BN layers. **c**, LEED pattern of as-grown hBN layers. **d**,**e**, Planar (**d**) and cross-sectional (**e**) HAADF-STEM images of hBN layers. The zone axis of (**e**) is zigzag direction of hBN layers.

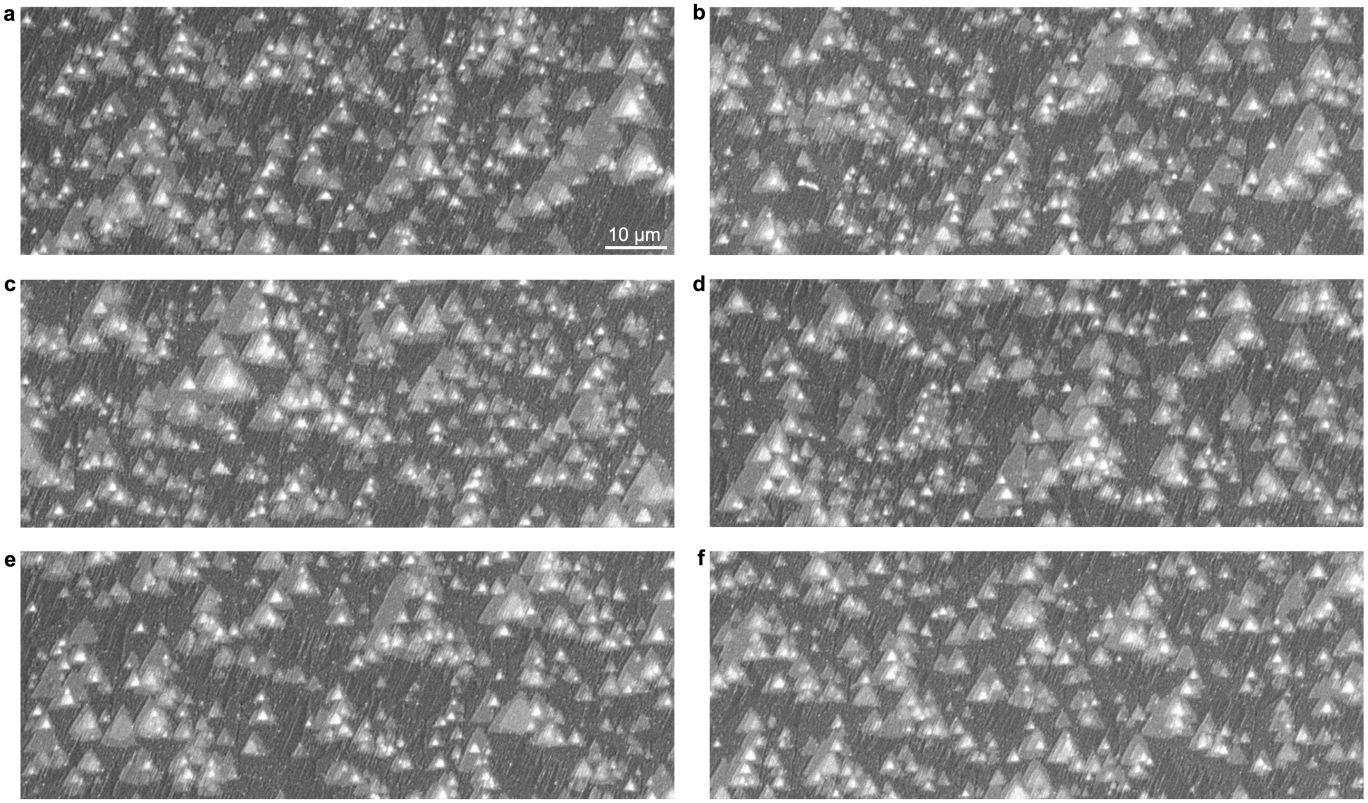

Extended Data Fig. 5 | SEM images of unidirectionally aligned rBN multilayer domains on Ni(520) substrates. All images are the same size.

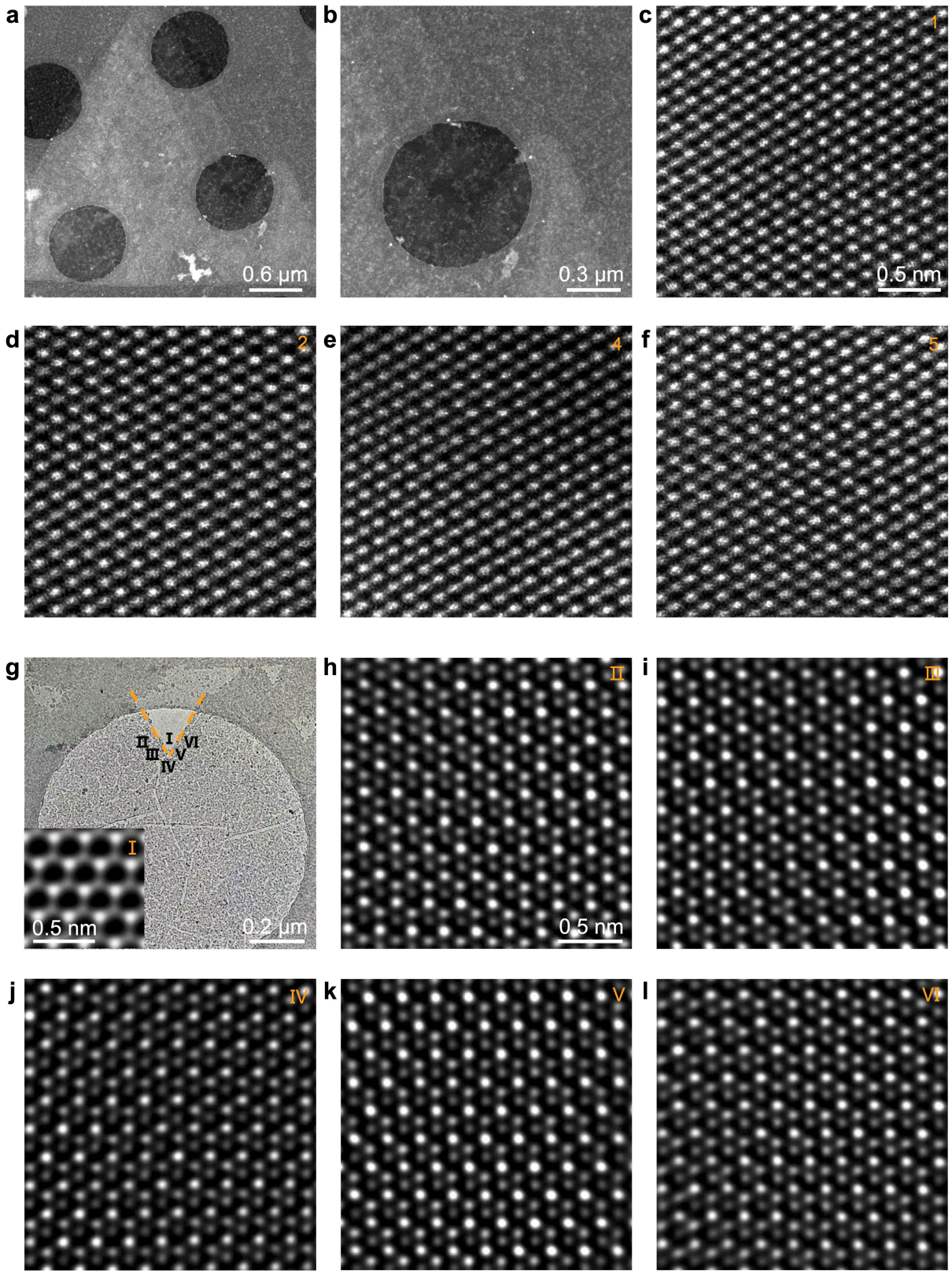

Extended Data Fig. 6 | More seamlessly stitching results. a,**b**, Pristine low-magnification STEM images of stitched region shown in Fig. 3c. **c**-**f**, Representative HAADF-STEM images collected at zones 1, 2, 4 and 5 marked in Fig. 3c. All images are the same size. **g**, Low-magnification TEM image obtained at the concave corner in the joint area of the first two layers of aligned rBN domains. Inset, the first layer BN that had been stitched into a continuous film. **h**-**l**, Representative HAADF-STEM images collected at zones II to VI marked in (**g**), showing the uniform lattice of stitched domains. All images are the same size.

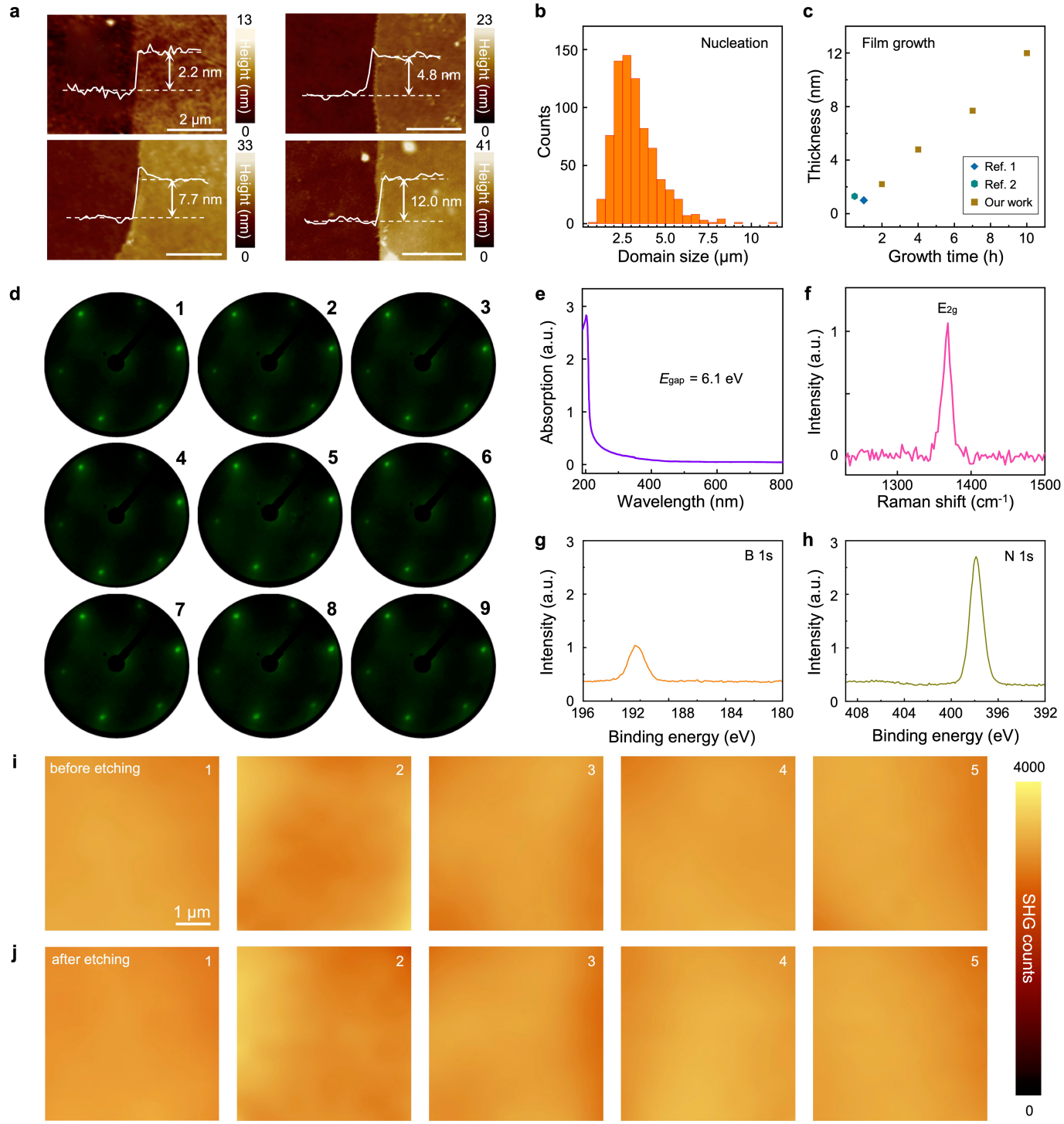

Extended Data Fig. 7 | Characterization of as-grown single-crystal rBN films. **a**, AFM height mappings of transferred rBN films with typical thicknesses in the range of 2.2–12 nm. **b**, Statistics of the side length of separated domains at the nucleation stage. The average domain size is calculated to be 3.1 μm. **c**, Statistics of the average film thickness, exhibiting the nearly-linear dependence on the growth time. The estimated growth rate at the film-formation stage is 1.15 nm/h, which is consistent with the previously reported values (ref. 1: Nature 2022, 88, 606; ref. 2: Nano Letters 2016, 16, 3360). **d**, LEED patterns of the as-grown rBN film collected at different positions. The threefold symmetric patterns with consistent orientation confirm the single-crystal nature of the rBN lattice. **e**-**h**, UV-vis spectrum with an absorption peak at 6.1 eV (**e**), Raman spectrum with a characteristic E_{2g} peak at 1368.5 cm^{-1} (**f**), and XPS spectra with B 1 s peak at 190.2 eV (**g**) and N 1 s peak at 397.9 eV (**h**), respectively, exhibiting the high quality of the as-grown rBN layers. **i**,**j**, *In-situ* SHG mappings of the rBN single-crystal films before (**i**) and after (**j**) etching, showing none of observed etched defect or thickness reduction. The same number corresponds to the same area, and all images are the same size.

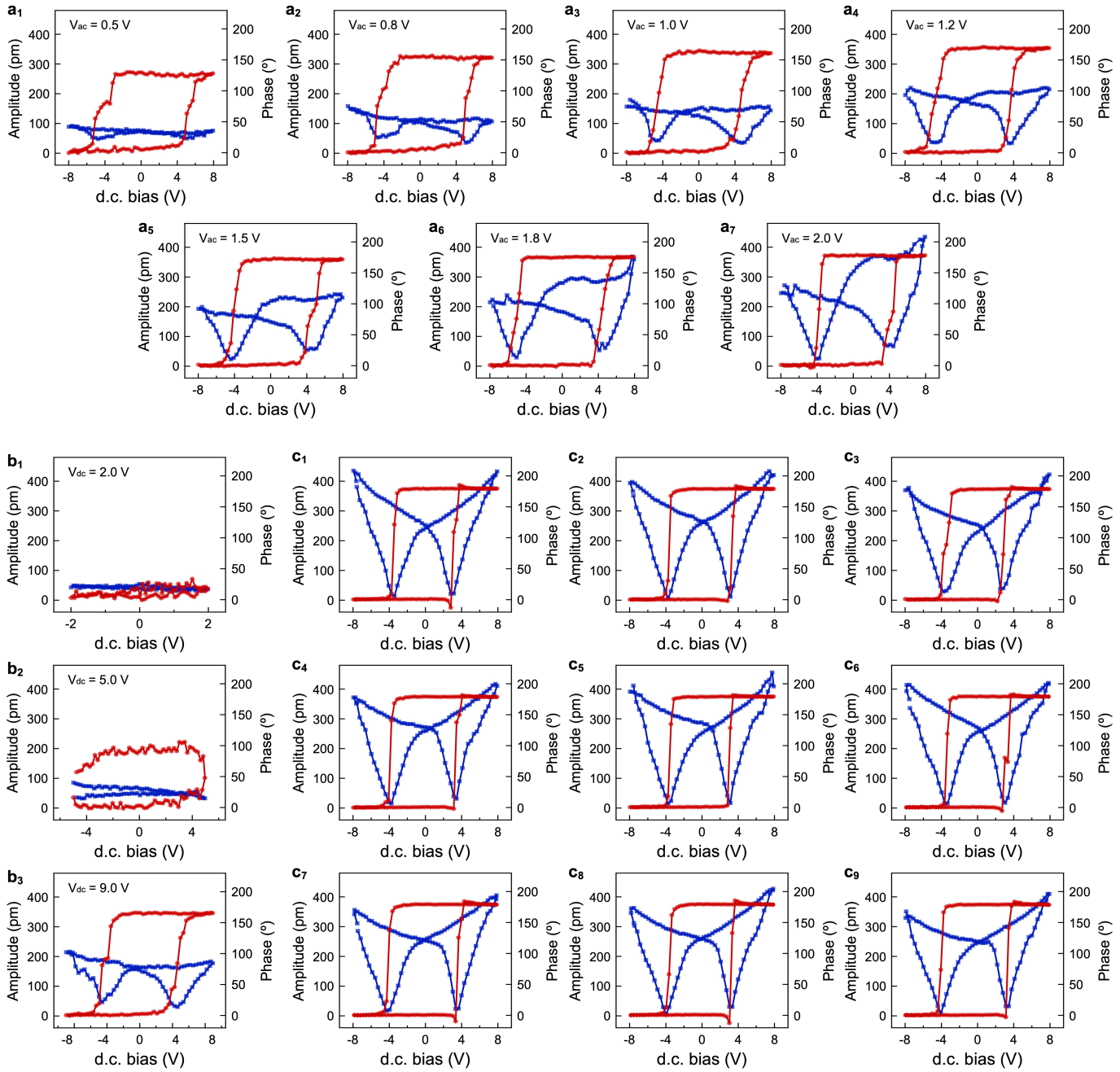

Extended Data Fig. 8 | Evolution of PFM response by using different a.c. (V_{ac}) and d.c. (V_{dc}) voltages. a,**b**, PFM signals with a fixed V_{dc} of 8 V and various V_{ac} of 0.8 V to 2.0 V (**a**), as well as a fixed V_{ac} of 1 V and V_{dc} ranging from 2.0 V to 9.0 V (**b**). The V_{dc}-dependent PFM hysteresis loops show that the rBN system has a specific coercive voltage (V_c). When V_{dc} is smaller than V_c in rBN, V_{dc} is not enough to switch the ferroelectric polarization, so a butterfly shaped curve in amplitude and 180° phase hysteresis are absent. In addition, the PFM loops show increasing amplitude and shrinking hysteresis window with increasing V_{ac} from 0.5 V to 2.0 V. **c**, PFM signals collected at different nine samples, indicating the reproducibility of ferroelectricity in rBN layers.

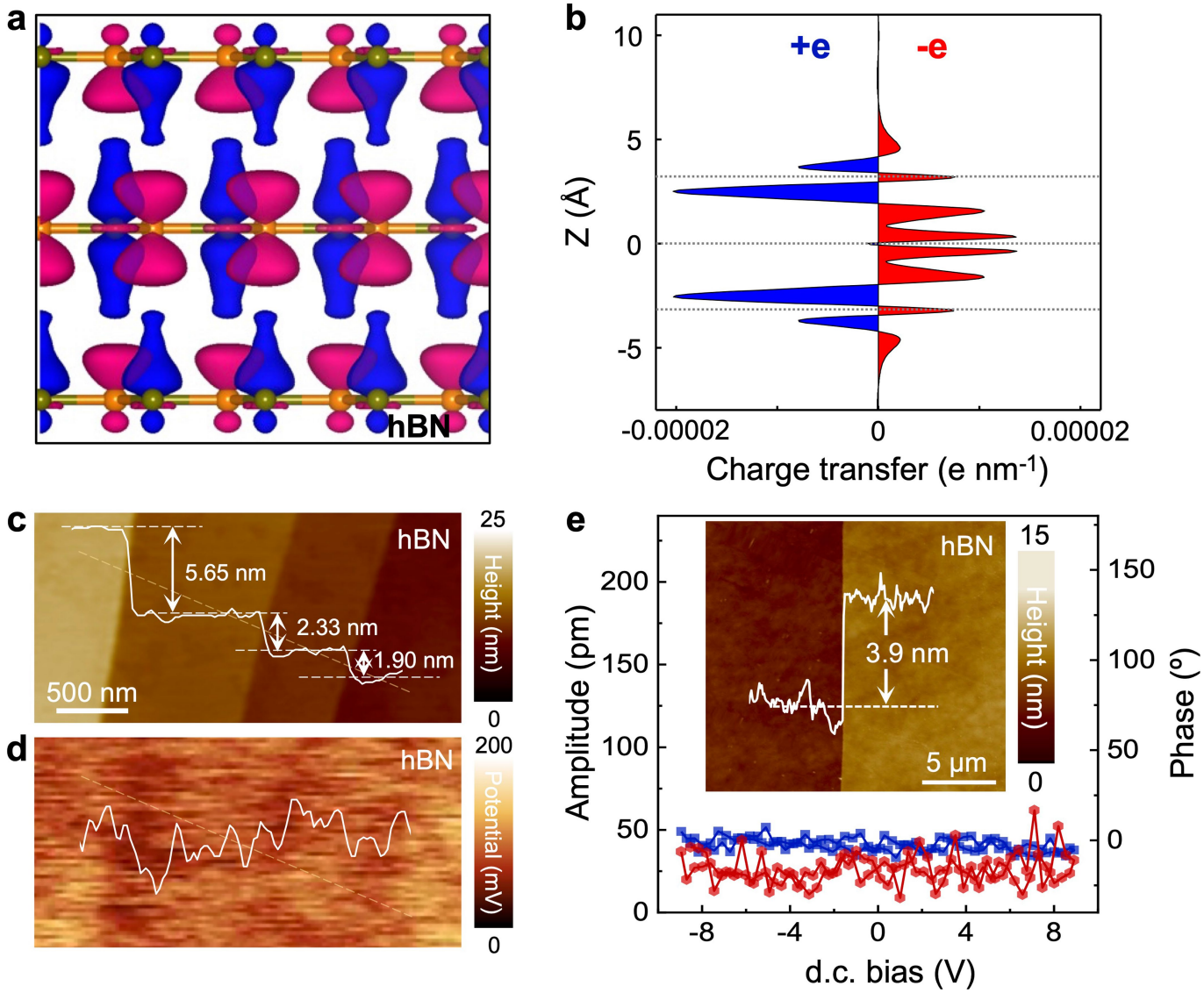

Extended Data Fig. 9 | Theoretical simulation and experimental measurements on hBN. a,**b**, Interlayer differential charge density (**a**) and the corresponding line profiles (**b**) of the exfoliated hBN flakes. **c**,**d**, AFM height mapping (**c**) and the corresponding KPFM mapping (**d**) measured on the exfoliated hBN flakes, showing no potential change of hBN with different thickness. The curve data were collected along the orange dashed lines. **e**, PFM measurements on exfoliated hBN flakes, showing the absence of ferroelectric responses. Inset, AFM height mapping of hBN with a typical thickness of 3.9 nm.

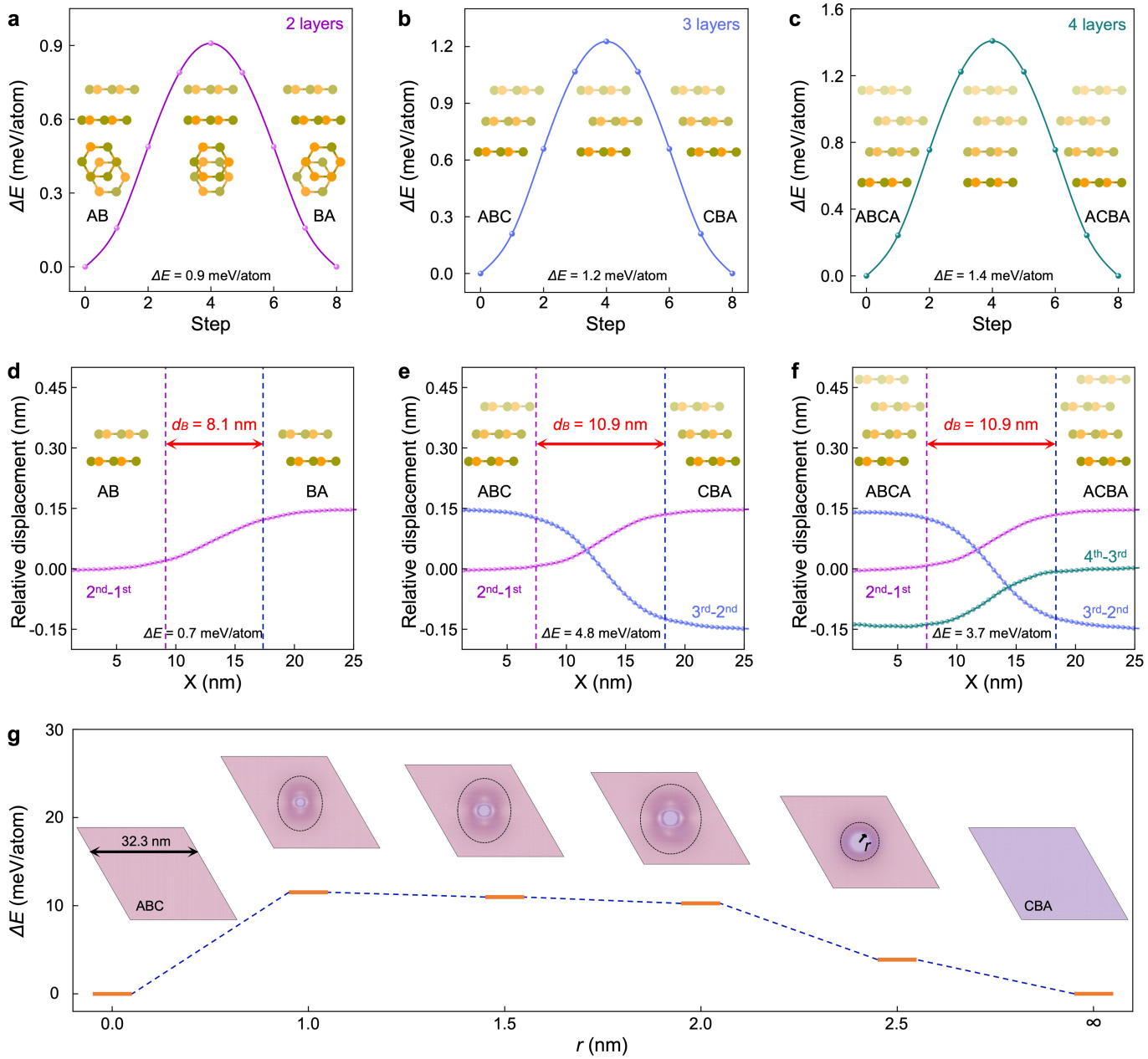

Extended Data Fig. 10 | Theoretical simulation of the switching barrier of the ferroelectric domains in rBN with 2–4 layers. a-c, Energy evolution of the bilayer (**a**), trilayer (**b**) and tetralayer (**c**) systems along with the sliding steps. **d-f**, Relative displacement curves between adjacent layers of rBN bilayer (**d**), trilayer (**e**) and tetralayer (**f**) under another sliding path. The dashed lines mark the corresponding domain boundary areas, and the switching barriers are also marked in the bottom of figures. The insets are different sliding paths and the orange and green balls represent the B and N atoms, respectively. **g**, Energy evolution with the nucleus propagation of rBN trilayer from ABC to CBA stacking sequence, where *r* represents the radius of nucleus. The CBA-stacked nucleus and fixed domain boundary region is marked by the black dashed lines.